Fast non-stationary deconvolution of ultrasonic beamformed images for nondestructive testing

Nans Laroche, Sébastien Bourguignon, Jérôme Idier, Ewen Carcreff, Aroune Duclos

Fast non-stationary deconvolution of ultrasonic beamformed images for nondestructive testing

Nans Laroche, Sébastien Bourguignon, Jérôme Idier, Ewen Carcreff, and Aroune Duclos

***Abstract*—This paper addresses high-resolution ultrasonic image reconstruction from Full Matrix Capture (FMC) data in the context of nondestructive testing (NDT). In order to reduce the numerical complexity, the time-domain data and ultrasonic model are projected into the image domain through a linear beamforming procedure. The resulting model is interpreted as a shift-variant convolution process, affected by non-stationary and colored noise. An interpolation procedure is built in order to account for the spatial variations of the resulting point spread function. Under the same methodological framework, an approximate whitening filter is proposed and incorporated in the forward model. Both constructions then allow fast computations and limited memory storage. Deconvolution is performed by minimizing the least-squares data misfit error, with a penalization term favoring sparsity and spatial continuity of the output images. Results with synthetic data show that the proposed approach gives performances close to the inversion of raw FMC data, while being computationally much more efficient. The method is finally applied to laboratory data for the inspection of a stainless steel block containing closely spaced and small side-drilled holes calibrated flaws. Successful detection and separation is achieved for flaws with diameters six times smaller than the wavelength, and distant from each other by four times less than the resolution limit given by the Rayleigh criterion.**

I. Introduction

A. State-of-the-art in NDT ultrasonic imaging

MODERN ultrasonic array probes contain a large number of transducers, offering high performance in terms of flexibility, speed and quality of inspection. In the field of non-destructive testing (NDT), the main advantage of the array-based ultrasonic modality is its ability to produce images from a single acquisition sequence through beamforming techniques [1]. Beamforming has been first hardware-implemented by applying different delay laws to the transducers in order to focus the beam at different locations of the inspected region. Nowadays, software-implemented beamforming is generally preferred, being obviously more flexible. In particular, the recent growth of Graphic Processing Units (GPU) capabilities has significantly improved the speed of beamforming algorithms, which can now compute hundreds of images per second [2].

Until recently, software-implemented beamforming was mostly performed using the Synthetic Aperture Focusing Technique (SAFT) [3], which consists in recording the pulse-echo responses of a moving single-element transducer. However, SAFT is becoming obsolete with the emergence of array probes, which enable more efficient data acquisition schemes. In medical ultrasound imaging, Plane Wave Imaging (PWI) [4] is now the standard method, where all elements emit plane wave fronts at different angles and receive synchronously. This technique maximizes the transmitted energy to the tissue at a high frame rate (up to several thousand images per second), which is critical in order to capture motion information [5].

In NDT, which is the target application area of this paper, obtaining high-resolution information is necessary in order to detect and characterize accurately possible flaws in the inspected piece [6], [7]. Typical examples of interest are the control of additively manufactured parts [8], [9], welds [10] or power generation units [11]. In such contexts, it is a priority to collect more exhaustive information than in medical imaging, at the price of slower acquisition rates. Therefore, a beamforming method of choice is the Total Focusing Method (TFM) [7], [12] applied to Full Matrix Capture (FMC), that is, the collection of all inter-element responses from an array probe. FMC has become a reference acquisition method for various typical applications in NDT. It is highly sensitive to small defects and is used for sub-wavelength reflectors detection [6]. It provides valuable information for the sizing and characterization of crack-like defects using diffraction and specular echoes [10], [13]–[15]. It is also efficiently used for the separation of close scatterers [16]–[19]. Let us also mention that this acquisition scheme was also used for particular applications in medical imaging, *e.g.,* blood flow estimation [20].

Due to its finite aperture, each transducer composing a multi-element probe has a limited bandwidth. Consequently, all *linear* beamforming techniques (SAFT, PWI, TFM) produce images of limited spatial resolution, in particular showing oscillations due to the shape of ultrasonic pulses. In order to improve the resolution and the contrast of ultrasonic images, previous works adopted an inverse problem approach [19], [21]–[23]. In [19], we proposed a linear forward model which relates the FMC data to the reflectivity map of the inspected region, accounting for the acoustic responses of the transducers. The corresponding inversion method is able to reconstruct highly resolved images, but at the price of a computationally expensive procedure due to the large size of FMC datasets, which makes it hardly compatible with some industrial NDT applications.

This paper proposes an inversion procedure which aims to preserve the resolution quality of FMC data inversion, while reducing the computation time, by reducing the size of the dataset. More precisely, we transfer the raw FMC data

N. Laroche and E. Carcreff are with the Phased Array Company (TPAC), Nantes, France (e-mail: nans.laroche@tpac-ndt.com).

N. Laroche, S. Bourguignon, and J. Idier are with the Laboratoire des Sciences du Numérique de Nantes (LS2N), Nantes, France.

A. Duclos is with the Laboratoire d'Acoustique de l'Université du Mans (LAUM), Le Mans, France.

model (*i.e.*, a collection of time-domain signals related to the unknown reflectivity inside the inspected medium) into the TFM beamformed image. A new forward model between the searched reflectivity map and the beamformed image is considered. The reconstruction of the reflectivity map then amounts to an image "deconvolution" problem, where the Point Spread Function (PSF) is spatially variant.

To our best knowledge, the principle of retrieving a reflectivity map from a beamformed image has never been considered in NDT, while it has already raised interest in medical imaging. In [24], [25], a regularized procedure is applied to the beamformed image, but no PSF is considered. The deconvolution of beamformed medical images is addressed in [26], where a shift-invariant PSF is calibrated from experimental data. In [27], an axially variant PSF is introduced by setting an analytical *ad-hoc* PSF model for each axial position. The recent contribution [28] also tackles non-stationary PSFs. It focuses on ultrafast ultrasound imaging, where datasets are obtained using compressed beamforming schemes. Unfortunately, it is hardly tranposable to the context of FMC imaging modality in NDT, since it would rely on repeated computations involving huge FMC datasets.

B. Contribution

The proposed method is specifically dedicated to ultrasonic imaging in NDT. We interpret the TFM beamformed image as the back-projection of the FMC data in the space domain. The resulting forward model directly relates the reflectivity map to the beamformed data through a spatially variant two-dimensional (2D) convolution, which accounts for both the time-domain impulse response of the transducers and the geometrical structure of the acquisition process. However, manipulating the set of exact PSFs at all points is not numerically feasible in realistic scenarios. Akin to previous contributions to shift-variant blur approximation in astronomical imaging [29], [30], we propose to accurately describe the PSF at all possible locations from the interpolation of a smaller set of reference PSFs, which are computed in two steps. First, synthetic ultrasonic data are generated considering pointwise excitations at different locations in the medium reflectivity, using the ultrasonic response model. Second, the TFM image is computed for each synthetic dataset, thereby identifying the PSF at each specific location.

A second specificity of our approach considers a forward model where the measurement noise affecting the raw FMC data is linearly transformed by the beamforming process. Such a "beamformed noise component" is not white, and its correlation structure is spatially varying. In the proposed inversion method, we account for this specific noise model, using the same methodology that was used to build the non-stationary convolution model. Finally, our inversion strategy relies on the minimization of a penalized least-squares criterion, where the penalization terms favor the presence of sparse regions of limited spatial extent.

The remainder of the paper is organized as follows. Section II introduces the data acquisition procedure, and states the corresponding model relating the FMC data to the unknown reflectivity map. In Section III, the output of the TFM procedure is related to the reflectivity image by a shift-variant 2D convolution model, for which a PSF interpolation model is built. The non-stationarity of the resulting error term is studied in Section IV, where an approximate whitening procedure is built. Then, our inversion procedure is detailed in Section V. The performance of the method in terms of image quality and of computing time is evaluated in Section VI on synthetic data. In Section VII, it is applied on NDT laboratory data acquired from a stainless steel block containing a set of close side-drilled holes. A discussion is finally given in Section VIII.

II. Full Matrix Capture data model

The Full Matrix Capture acquisition modality collects the ultrasonic signals that are emitted independently by each transducer and received by all of them. For an array probe containing N_{el} transducers, N_{el}^2 A-scan signals $y_{a,b}(t)$ are recorded, where a and b respectively index the emitter and the receiver. An example of (partial) FMC data is shown in Figure 1, corresponding to the inspection of the specimen that will be described in the experimental Section VII. Typical A-scans extracted from this data set are shown in Figure 2. We can identify frontwall and backwall echoes, as well as the signature of close side-drilled holes generating mixed echoes.

Each A-scan can be modeled as the superposition of time-delayed echoes of the ultrasonic wave that propagates into the medium, where each echo corresponds to the reflection at each point of the medium, weighted by the corresponding reflectivity value [31]. Akin to [19], we adopt the following model for the FMC data:

$$\boldsymbol{y} = \mathbf{H}_t \boldsymbol{o} + \boldsymbol{n}_t, \tag{1}$$

where $\boldsymbol{y} \in \mathbb{R}^{N_{\text{el}}^2 N_t}$ is a column vector gathering all discrete-time A-scans (each of which has N_t samples), $\boldsymbol{o} \in \mathbb{R}^{N_x N_z}$ is the column vector containing the reflectivity value at any point of an $N_x \times N_z$ discrete grid in the medium, and $\boldsymbol{n}_t \in \mathbb{R}^{N_{\text{el}}^2 N_t}$ stands for noise and model errors. Matrix $\mathbf{H}_t \in \mathbb{R}^{N_{\text{el}}^2 N_t \times N_x N_z}$ is the waveform matrix containing the pulse waveforms shifted at the corresponding times of flight for all combinations of A-scans and pixels.

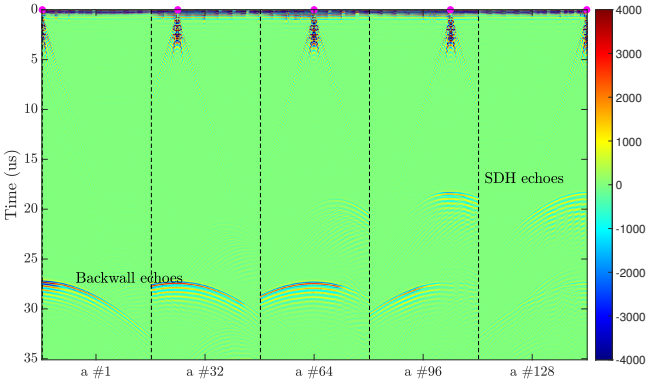

Fig. 1. Typical FMC data in NDT, obtained with a 128-element probe (partial). Five blocks are represented, corresponding to the 128 collected signals after emission by transducer 1, 32, 64, 96 and 128.

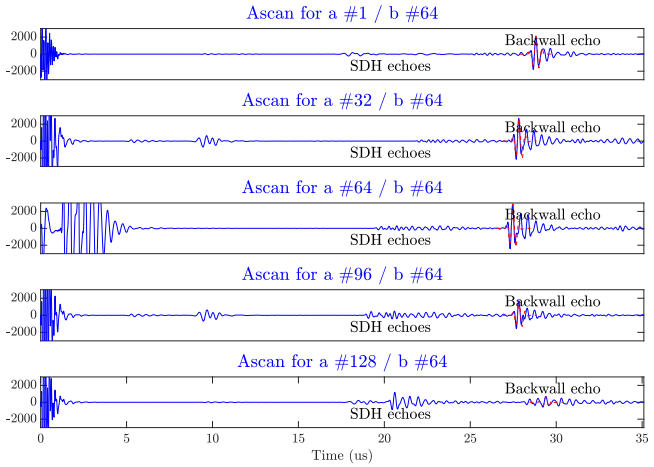

Fig. 2. Some time-domain signals from the FMC data set in Figure 1. In red, the estimated elementary waveform that will be used in the model (see Section VII).

III. Forward shift-variant convolution model on the beamformed image

In [19], an inversion procedure was proposed to estimate the reflectivity map $\boldsymbol{o}$ from the data $\boldsymbol{y}$ based on model (1), allowing high-resolution reconstructed images. However, dealing with the huge FMC data $\boldsymbol{y}$ makes this method impractical in many NDT situations, where relatively high-speed inspection may be necessary. In this section, we reduce the data size, by considering the image produced by the Total Focusing Method [12] as the new input of our reconstruction method.

A. Total Focusing Method

The Total Focusing Method is the standard beamforming procedure from FMC data. We consider the (x, z) coordinate system (see for example Figure 3), where emitter a and receiver b are respectively located at $(x_a, 0)$ and $(x_b, 0)$. In the standard configuration where the probe is in contact with the medium to inspect, the travel time from the emitter a to a given location $\boldsymbol{r} = (x, z)$, augmented with the return travel time to receiver b, reads:

$$\tau(\boldsymbol{r}, x_a, x_b) = \frac{\sqrt{(x-x_a)^2+z^2} + \sqrt{(x-x_b)^2+z^2}}{c}, \quad (2)$$

where c is the ultrasonic velocity. The TFM image at pixel $\boldsymbol{r}$ is then defined by adding all signals delayed by the corresponding times of flight [12]:

$$O_{\text{TFM}}(\boldsymbol{r}) := \sum_{a=1}^{N_{\text{el}}} \sum_{b=1}^{N_{\text{el}}} y_{a,b}\big(\tau(\boldsymbol{r}, x_a, x_b)\big). \quad (3)$$

In discrete form, this reads:

$$\boldsymbol{o}_{\text{TFM}} = \mathbf{B}\boldsymbol{y} \quad (4)$$

where $\boldsymbol{o}_{\text{TFM}} \in \mathbb{R}^{N_x N_z}$ collects the values of the TFM image in a column vector, and the binary matrix $\mathbf{B} \in \{0;1\}^{N_x N_z \times N_{\text{el}}^2 N_t}$ will be called the beamforming operator: for each pixel of the TFM reconstruction grid, the corresponding row in $\mathbf{B}$ selects the indices corresponding to the appropriate (rounded) times of flight in each A-scan according to Eq. (2).

B. Shift-variant convolution model

We consider the projection of the FMC data model into the spatial domain using the TFM beamforming operator. Combining Eqs. (1) and (4), we obtain:

$$\boldsymbol{o}_{\text{TFM}} = \mathbf{H}_s \boldsymbol{o} + \boldsymbol{n}_s, \quad (5)$$

with $\mathbf{H}_s := \mathbf{B}\mathbf{H}_t$ and $\boldsymbol{n}_s := \mathbf{B}\boldsymbol{n}_t$. Matrix $\mathbf{H}_s \in \mathbb{R}^{N_x N_z \times N_x N_z}$ is now a square operator converting the discretized reflectivity map into the TFM image. Considering model (5) instead of (1) relies on the idea that the loss of information between the FMC data and the TFM image is limited, and that it can be partly compensated by accurately modeling the resulting PSF and the noise statistical properties. Each column of $\mathbf{H}_s$ represents the PSF at a given pixel, that is, the TFM image of a pointwise reflector at this location. Due to the acquisition geometry, the shape of the PSF is different for each pixel location, that is, the product $\mathbf{H}_s\boldsymbol{o}$ represents a shift-variant 2D convolution operation.

Figure 3 shows typical PSFs obtained at four different locations in a 30 mm $\times$ 30 mm image. The time-domain transducer pulse is a symmetric Gaussian wavelet [32], with central frequency $f_0 = 5\,\text{MHz}$ and bandwidth ratio (the frequency bandwidth over f_0) at $-3\,\text{dB}$ equal to 0.4. The sound velocity is 5000 m/s, such that the wavelength in the material is $\lambda = c/f_0 = 1$ mm. Synthetic data were generated with a 64-element array probe, with an inter-element spacing equal to $\lambda/2 = 0.5$ mm. The reflectivity image was composed of four point sources located at $(x, z) = (7.5, 7.5)$, $(7.5, 22.5)$, $(22.5, 7.5)$, and $(22.5, 22.5)$ mm, then yielding the four PSFs at these pixels. As expected, the PSF is wider as the depth increases, and its orientation depends on the pixel location.

C. PSF interpolation

Although the PSF can be computed at any point of the image, computing one PSF per pixel would not be reasonable nor really useful. In [28], a model accounting for an exact PSF at each location of the reconstruction grid was proposed. However, this model relies on the data propagation operator, which would be too expensive computationally with large-size FMC data. Here, we rather rely on the fact that the PSF variations between close pixels are smooth (see the examples in Figure 3). Consequently, an interpolation model can be used to approximate the PSF shape at any location from a small number of reference PSFs with controlled accuracy.

The interpolation model proposed in this paper is inspired by previous works in Astrophysics [29], [30]. In the following, we denote by $\boldsymbol{r}_n$ the coordinate vector for the pixel indexed by n in a vectorized image. We first define a set of reference PSFs, say h_i^{ref}, $i \in [\![1, N^{\text{ref}}]\!]$, corresponding to the PSFs computed at pixels $\boldsymbol{r}_i$. Moreover, we introduce weight maps w_i to modulate their contributions to PSF interpolation. That is, the PSF at any pixel $\boldsymbol{r}_n$, say $h_{\boldsymbol{r}_n}$, is approximated as follows:

$$h_{\boldsymbol{r}_n}(\boldsymbol{r}) \approx \sum_{i=1}^{N^{\text{ref}}} w_i(\boldsymbol{r}_n) h_i^{\text{ref}}(\boldsymbol{r}). \quad (6)$$

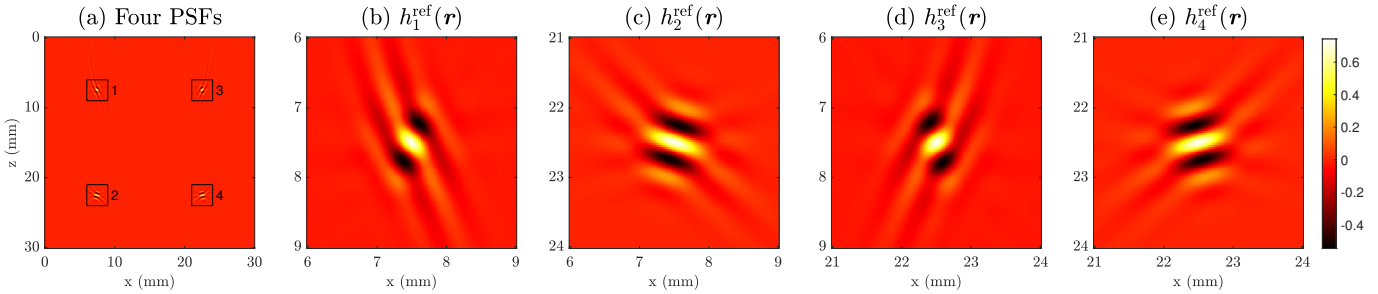

Fig. 3. Variability of the PSF corresponding to model (5). (a): four PSFs computed at several pixels of the reconstruction grid (centered on the black squares). (b)-(e): zooms on the corresponding zones.

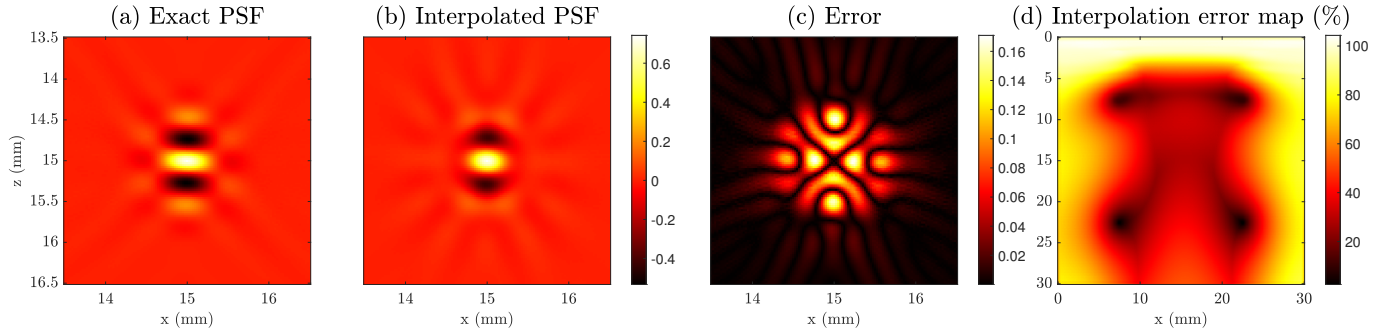

Fig. 4. PSF interpolation: illustration on the synthetic example in Figure 3. (a): exact PSF $h_{\boldsymbol{r}_c}(\boldsymbol{r})$ at the center $\boldsymbol{r}_c$ of the image. (b): interpolation by $\widetilde{h}_{\boldsymbol{r}_c}(\boldsymbol{r}) = \sum_{i=1}^{4} w_i(\boldsymbol{r}_c) h_i^{\text{ref}}(\boldsymbol{r})$. (c): interpolation error image $h_{\boldsymbol{r}_c} - \widetilde{h}_{\boldsymbol{r}_c}(\boldsymbol{r})$. (d): relative ℓ_2-norm interpolation error map $\|h_{\boldsymbol{r}_n} - \widetilde{h}_{\boldsymbol{r}_n}\|_2 / \|h_{\boldsymbol{r}_n}\|_2$ for all pixels $\boldsymbol{r}_n$.

Here, we use the Inverse Distance Weighting (IDW) model [29]:

$$w_i(\boldsymbol{r}_j) = \delta_{i,j} \qquad \forall\, j \in [\![1, N^{\text{ref}}]\!], \tag{7a}$$

$$w_i(\boldsymbol{r}_n) = \frac{\|\boldsymbol{r}_n - \boldsymbol{r}_i\|_2^{-1}}{\sum_{j=1}^{N^{\text{ref}}} \|\boldsymbol{r}_n - \boldsymbol{r}_j\|_2^{-1}} \qquad \forall\, n \notin [\![1, N^{\text{ref}}]\!], \tag{7b}$$

where $\|\cdot\|_2$ denotes the Euclidean norm.

An example is shown in Figure 4, using the four PSFs introduced in Section III-B as references. Figures 4(a)-(c) respectively show the exact PSF at the center of the image, its interpolation and the corresponding error. The main lobes are quite accurately modeled, and the relative error is approximately 30%. Finally, Figure 4(d) shows the relative PSF interpolation error at each point of the image. It is less than 30% at the center part of the image (where the acoustic field is homogeneous). Due to the inspection geometry, the PSFs at the top and on the sides of the image suffer from distortions that are more difficult to consider. These inconsistencies are related to the TFM process. Indeed, the acoustic field is not homogeneous on the sides of the grid corresponding to the edges of the probe. The PSF spatial variations are also stronger in the near surface area, therefore reducing the interpolation accuracy. However, this has a limited impact since the top of the image is strongly affected by the surface echo in contact inspection, and is usually discarded in the image analysis.

Now, let $O(\boldsymbol{r})$ denote the reflectivity value at pixel with coordinates $\boldsymbol{r}$. From model (6), the spatially-variant 2D convolution at a given pixel $\boldsymbol{r}_n$ reads:

$$\begin{aligned}\sum_{\boldsymbol{r}} h_{\boldsymbol{r}}(\boldsymbol{r}_n - \boldsymbol{r}) O(\boldsymbol{r}) &\approx \sum_{\boldsymbol{r}} \sum_{i=1}^{N^{\text{ref}}} w_i(\boldsymbol{r}) h_i^{\text{ref}}(\boldsymbol{r}_n - \boldsymbol{r}) O(\boldsymbol{r}) \\ &= \sum_{i=1}^{N^{\text{ref}}} \sum_{\boldsymbol{r}} h_i^{\text{ref}}(\boldsymbol{r}_n - \boldsymbol{r}) O^{w_i}(\boldsymbol{r}) \\ &= \left(\sum_{i=1}^{N^{\text{ref}}} h_i^{\text{ref}} * O^{w_i} \right)(\boldsymbol{r}_n), \end{aligned} \tag{8}$$

where $O^{w_i}(\boldsymbol{r}) := O(\boldsymbol{r}) w_i(\boldsymbol{r})$ and $*$ denotes the 2D convolution. The forward model (5) can then be evaluated by summing N^{ref} 2D convolution products, applied to the reflectivity images that have been weighted by the corresponding maps.

IV. Colored, non-stationary, noise model

The uncertainty term $\boldsymbol{n}_t$ in the time-domain signal model (1) stands for model errors and electronic noise affecting FMC data. In NDT, it is reasonable to model them as centered Gaussian white noise if the medium is homogeneous, *i.e.*, if the size of the material grain is small compared to the wavelength. The covariance matrix of $\boldsymbol{n}_t$ reads $\text{Cov}(\boldsymbol{n}_t) = \mathbb{E}[\boldsymbol{n}_t \boldsymbol{n}_t^t] = \sigma^2 \mathbf{I}$, with σ^2 the noise power and $\mathbf{I}$ the identity matrix of size $N_x N_z$. When dealing with the projected model in the image domain proposed in Eq. (5), the noise term $\boldsymbol{n}_s$ is filtered by the beamforming operator $\mathbf{B}$, therefore its covariance matrix reads $\boldsymbol{\Gamma}_s = \sigma^2 \mathbf{B}\mathbf{B}^t$. From the definition of matrix $\mathbf{B}$ in

Section III-A, one can show that the element (i,j) of matrix $\mathbf{\Gamma}_s$ is:

$$\begin{aligned}\gamma(\boldsymbol{r}_i,\boldsymbol{r}_j) =&\sigma^2 \text{ Card } S_{ij}, \text{with}\\ S_{ij} :=&\big\{(a,b)\in[\![1,N_{\text{el}}]\!]^2 \text{ such that}\\ &[\tau(\boldsymbol{r}_i,x_a,x_b)F_s] = [\tau(\boldsymbol{r}_j,x_a,x_b)F_s]\big\},\end{aligned} \tag{9}$$

where F_s is the sampling frequency, $\tau(\boldsymbol{r},a,b)$ is the flight time defined in Eq. (2), and notation $[\cdot]$ rounds to the closest integer. S_{ij} denotes the set of emitter-receiver pairs for which the (rounded) travel times through pixels $\boldsymbol{r}_i$ and $\boldsymbol{r}_j$ are equal. The noise process $\boldsymbol{n}_s$ is clearly not white, but also non-stationary, because the sets S_{ij} depend on the acquisition geometry.

A classical approach to deal with colored noise considers a "pre-whitening" procedure [33], [34] in order to retrieve a simpler case, where standard techniques based on the white noise assumption can be used. That is, we seek a whitening operator represented by matrix $\mathbf{G}_s \in \mathbb{R}^{N_xN_z\times N_xN_z}$, so that model (5) becomes:

$$\mathbf{G}_s\boldsymbol{o}_{\text{TFM}} = \mathbf{G}_s\mathbf{H}_s\boldsymbol{o} + \mathbf{G}_s\boldsymbol{n}_s, \tag{10}$$

where $\mathbf{G}_s\boldsymbol{n}_s$ is a white noise process. Computing the ideal whitening operator would require the computation of the square root of $\mathbf{\Gamma}_s^{-1}$, which is not easily usable in our case, in particular because $\mathbf{\Gamma}_s$ is a huge matrix with no specific structure.

In order to define an efficient whitening procedure that takes into account the spatial variability of the noise, we propose to build an approximate spatially-variant whitening filter, in a similar way to the PSF interpolation procedure defined in Section III-C. First, we build noise covariance functions that are defined *locally*, at the same pixels as the reference PSFs. To do so, we define the spatial covariance function $\widehat{\gamma}_i^{\text{ref}}, i \in [\![1,N^{\text{ref}}]\!]$ at the reference pixel $\boldsymbol{r}_i$, from the noise covariance between pixel $\boldsymbol{r}_i$ and any other pixel—defined in Eq. (9)—as:

$$\widehat{\gamma}_i^{\text{ref}}(\boldsymbol{r}) := \tfrac{1}{2}\left(\gamma(\boldsymbol{r}_i,\boldsymbol{r}_i+\boldsymbol{r}) + \gamma(\boldsymbol{r}_i,\boldsymbol{r}_i-\boldsymbol{r})\right) \text{ for } \boldsymbol{r}\neq\mathbf{0}, \tag{11a}$$

$$\widehat{\gamma}_i^{\text{ref}}(\mathbf{0}) := \gamma(\boldsymbol{r}_i,\boldsymbol{r}_i) + \eta. \tag{11b}$$

Eq. (11a) ensures that the covariance function is symmetric, so that the power spectral density, say $\mathcal{F}\widehat{\gamma}_i^{\text{ref}}$ (the Fourier transform of $\widehat{\gamma}_i^{\text{ref}}$), is real-valued. Then, if $\mathcal{F}\widehat{\gamma}_i^{\text{ref}}(\boldsymbol{\nu})$ takes negative values, the addition of $\eta := -\min_{\boldsymbol{\nu}} \mathcal{F}\widehat{\gamma}_i^{\text{ref}}(\boldsymbol{\nu})$ in (11b) ensures that $\mathcal{F}\widehat{\gamma}_i^{\text{ref}}(\boldsymbol{\nu}) \geq 0$ for any spatial frequency $\boldsymbol{\nu}$. Finally, we now define the local whitening filter at pixel $\boldsymbol{r}_i$, whose transfer function is obtained by Wiener filtering:

$$\mathcal{F}g_i^{\text{ref}}(\boldsymbol{\nu}) := \frac{\sqrt{\mathcal{F}\widehat{\gamma}_i^{\text{ref}}(\boldsymbol{\nu})}}{\mathcal{F}\widehat{\gamma}_i^{\text{ref}}(\boldsymbol{\nu}) + \mu}, \quad \mu>0, \tag{12}$$

where g_i^{ref} denotes the corresponding impulse response. In order to account for non-stationary noise, we finally propose to replace the spatially-variant PSF model in Section III-C by the *whitening PSF* model, where reference PSFs h_i^{ref} are substituted for

$$f_i^{\text{ref}} := g_i^{\text{ref}} * h_i^{\text{ref}}. \tag{13}$$

Figure 5 shows the reference whitening filters g_i^{ref} associated to the four PSFs h_i^{ref} introduced in Section III-C and represented in Figure 3. Such whitening filters show similar characteristics to those of the PSFs h_i^{ref} (similar orientations, slow spatial variations), although with a smaller spatial extension.

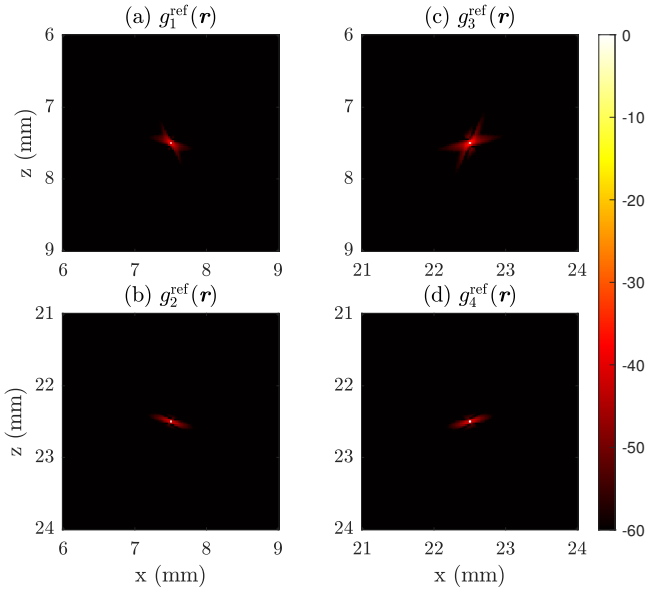

Fig. 5. Impulse responses of the whitening filters g_i^{ref} at the same locations as the four PSFs in Figure 3. The absolute value is displayed in logarithmic scale for a better visibility.

V. Inversion procedure

We now design an inversion method to retrieve the reflectivity map $\boldsymbol{o}$ from the TFM image $\boldsymbol{o}_{\text{TFM}}$. Such an inverse problem is ill-posed since the TFM image lacks information (in particular at high frequencies), due to the limited bandwidth of the ultrasonic transducers. We adopt a standard regularization strategy, where the ultrasonic image is obtained by minimizing the penalized least-squares criterion:

$$\boldsymbol{o}_s = \arg\min_{\boldsymbol{o}} J_{\text{LS}}(\boldsymbol{o}) + \phi_{\text{reg}}(\boldsymbol{o}). \tag{14}$$

The two terms in Eq. (14) are discussed hereafter.

From the whitening procedure described in Section IV and with similar notations, the whitened forward model (10) can be approximated by:

$$\boldsymbol{o}_{\text{TFM}}^{\mathcal{W}} = \mathbf{H}_s^{\mathcal{W}}\boldsymbol{o} + \boldsymbol{n}_s^{\mathcal{W}}, \tag{15}$$

where:

- $\boldsymbol{o}_{\text{TFM}}^{\mathcal{W}}$ is the vectorized form of the approximate whitened TFM image $O_{\text{TFM}}^{\mathcal{W}} := \sum_{i=1}^{N^{\text{ref}}} g_i^{\text{ref}} * O_{\text{TFM}}^{w_i}$, where $O_{\text{TFM}}^{w_i}(\boldsymbol{r}) := O_{\text{TFM}}(\boldsymbol{r})w_i(\boldsymbol{r})$;
- $\mathbf{H}_s^{\mathcal{W}}\boldsymbol{o}$ is the vectorized form of the approximate whitened forward model operator applied to the reflectivity image, that is, $\displaystyle\sum_{i=1}^{N^{\text{ref}}} f_i^{\text{ref}} * O^{w_i}$.

By construction, the noise term $\boldsymbol{n}_s^{\mathcal{W}}$ can now be considered as stationary and white, with covariance matrix equal to $\mathbf{I}$. Then, considering the standard least-squares criterion:

$$J_{\text{LS}}(\boldsymbol{o}) := \left\|\boldsymbol{o}_{\text{TFM}}^{\mathcal{W}} - \mathbf{H}_s^{\mathcal{W}}\boldsymbol{o}\right\|_2^2 \tag{16}$$

is statistically founded.

In NDT, sparsity-enhancing regularization is often considered [19], [21], [22]. It is adapted to the detection of few reflectors in homogeneous media, and it improves the resolution by introducing high-frequency information in the solution. Here, we also introduce spatial smoothness in the solution in order to enhance the reconstruction of reflectors with some spatial extension. Hence, we define the penalization function $\phi_{\text{reg}}(\boldsymbol{o})$ as:

$$\phi_{\text{reg}}(\boldsymbol{o}) = \mu_1 \left\|\boldsymbol{o}\right\|_1 + \mu_2 \left\|\mathbf{D}\boldsymbol{o}\right\|_2^2, \quad \mu_1, \mu_2 > 0, \tag{17}$$

where $\mathbf{D}\boldsymbol{o}$ is the image gradient. The ℓ_1-norm term favors sparsity, and the second term enhances spatial smoothness. It can be shown that for any $\mu_1 \geq \mu_1^{\max}$ with

$$\mu_1^{\max} := 2 \left\|(\mathbf{H}_s^{\mathcal{W}})^t \boldsymbol{o}_{\text{TFM}}^{\mathcal{W}}\right\|_\infty, \tag{18}$$

the reconstructed image is identically zero, whatever the value of μ_2 [19]. In practice, we set μ_1 to a fraction of $\mu_1^{\max}$ and μ_2 is set to a small positive value (see the experimental Sections VI and VII).

The minimization of the cost function in Eq (14) resorts to convex, non-smooth, optimization, which is performed in this paper with the FISTA algorithm (Fast Iterative Shrinkage Thresholding Algorithm) [35], which is a popular iterative algorithm for such kind of problems. It requires the evaluation of the forward $\mathbf{H}_s^{\mathcal{W}}\cdot$ and adjoint $(\mathbf{H}_s^{\mathcal{W}})^t\cdot$ operators at each iteration. Following the interpolation procedures described in Sections IV and V, both operations essentially resort to computing N^{ref} 2D convolution products. In this work, we exploit the fact that the practical range of each PSF is limited to a small area, so that evaluation of convolution products in the space domain turns out to be more efficient than computations based on two-dimensional Fast Fourier Transform (FFT). The FISTA algorithm is implemented in Matlab and the convolution products are computed using CPU-based (C++) and GPU-based (CUDA) implementation. Indeed, since the reconstructed images are very sparse, forward operations are more efficiently computed with CPU, whereas non-sparse adjoint operations advantageously benefit from GPU implementation.

VI. Results with synthetic data

In this section, the proposed method is evaluated on synthetic data. Section VI-A first describes the simulation setup. Then the relevance of the proposed model (PSF interpolation, noise prewhitening) is studied in Subsection VI-B. Its impact on the computation time is addressed in Subsection VI-C.

A. Simulation setting

We consider a synthetic array probe made of 64 elements with inter-element distance equal to $\lambda/2$, with wavelength $\lambda = 1$ mm. The medium is inspected in contact and contains 25 pairs of close pointwise reflectors, separated horizontally from $d_{\text{F}} = \lambda/2 = 0.5\,\text{mm}$. Each pair of reflectors is centered on a grid with coordinates $(x, z) \in [5, 10, 15, 20, 25]$ mm $\times$ $[5, 10, 15, 20, 25]$ mm. The pixel size is 0.1×0.1 mm^2. The synthetic reflectivity map equals 1 at the reflectors location and 0 elsewhere. The FMC data are generated with model (1), where the transducer impulse response is a symmetric Gaussian wavelet [32], with central frequency $5\,\text{MHz}$ and bandwidth ratio equal to 0.4. White Gaussian noise is added, with signal-to-noise ratio $\text{SNR} := 10\log_{10}\left\|\mathbf{H}_t\boldsymbol{o}\right\|_2^2 / N_{\text{el}}^2 N_t \sigma^2 = 10$ dB.

We compare the following deconvolution methods of the TFM image obtained by:

- using one single PSF computed at the center of the grid and assuming white noise in the TFM data model (5), named Deconv$_1$;
- using four reference PSFs computed on a $3\,\text{mm} \times 3\,\text{mm}$ map (see Figure 3) and the PSF interpolation model defined in Section III-C, still with the white noise assumption for model (5), named Deconv$_4$;
- using the former PSF interpolation model, but now with the colored noise assumption and the whitened model in (15), named Deconv$_4^{\mathcal{W}}$.

In all experiments in this section, the regularization parameter μ_1 is set to $0.8\left\|\mathbf{H}^t\boldsymbol{o}_{\text{TFM}}\right\|_\infty$, where $\mathbf{H}$ denotes the appropriate forward operator in each case, that is, using on single centered PSF for Deconv$_1$, using four reference PSFs for Deconv$_4$ and Deconv$_4^{\mathcal{W}}$. In the latter case, the whitened model is used and the whitened TFM image $\boldsymbol{o}_{\text{TFM}}^{\mathcal{W}}$ is considered instead of $\boldsymbol{o}_{\text{TFM}}$. We also consider the inversion procedure proposed in [19] using the full FMC data set $\boldsymbol{y}$ and based on model (1)— the same penalization framework is used— which can be viewed as the reference inverse solution, since there is no information loss in the model. In that case, we similarly set $\mu_1 = 0.8\left\|\mathbf{H}_t^t\boldsymbol{y}\right\|_\infty$. Parameter μ_2 is always set to 0, since only pointwise reflectors are considered in this section.

Optimization of criterion (14) is run with the FISTA procedure until the relative norm between successive iterates becomes smaller than 0.1%.

B. Impact of PSF variability and colored noise models

The TFM image is shown in Figure 6, and the reconstructed image lines at the five exact depths of the reflectors are shown in Figure 7 (for better visibility, results are split in two panels).

All methods improve the resolution of the TFM image and are able to separate some of the pairs of reflectors. Deconv$_1$ achieves good results at the center of the imaging area, where the (invariant) PSF model is the most accurate, but misses detections on both edges and at the top of the image. Including the PSF interpolation model with Deconv$_4$ improves the detection and separation of the reflectors, in particular at low depth where the PSF varies more strongly, but some detections are still missed at the edges of the scene. Finally, the inversion that includes both the PSF interpolation and the whitening procedure is able to correctly reconstruct all the reflectors pairs.

This experiment was repeated ten times, with different noise realizations with $\text{SNR} = 10$ dB. The following metrics were computed, where quantities were averaged over the data realizations and over the 25 pairs of reflectors:

- The **position error** measures the distance between the detected and the true reflectors. We consider that a

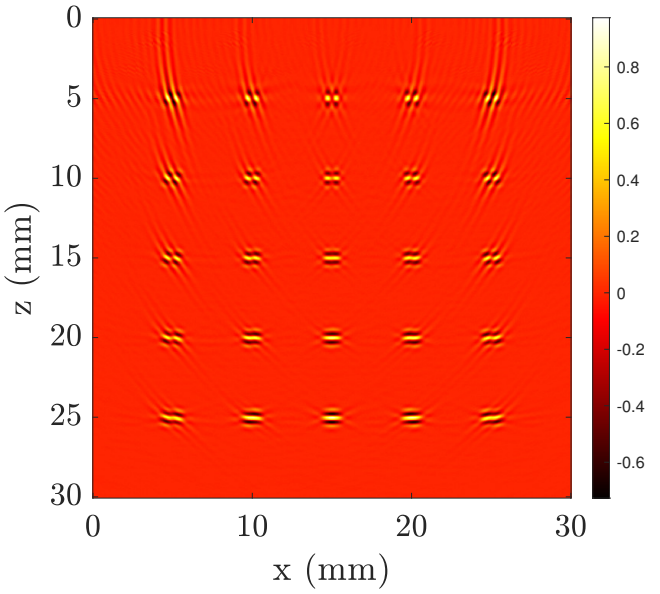

Fig. 6. TFM image for a synthetic scene composed of 25 pairs of close reflectors.

pointwise reflector is detected if a local maximum in the reflectivity map is distant from the true reflector by less than $d_F/4$, that is, no farther than one of the pixels neighboring the true location. If no reflector is detected, a maximum distance is set to $d_F/2$.

- The **Peak to Center Intensity Difference (PCID)** [18] computes the difference in amplitude between the maximum of the estimated reflectivity due to the two reflectors and the minimum in the area between them, in dB. If the two reflectors are not separated, then the PCID is set to 0. Since the image is sparse, an infinite PCID may be reached. In this case, the value is set to -50 dB.
- The **resolution capability** indicator measures the ratio of resolved pairs of reflectors, considering that the pair is resolved if the corresponding PCID is below -6 dB [18].
- The **quadratic error** corresponds to the ℓ_2-norm reconstruction error, expressed as a percentage of the ℓ_2 norm of the true reflectivity map.
- Finally, the **amplitude** of the estimated reflectivity at the reflectors locations is computed, as a percentage of the true reflectivity value.

Results are gathered in Figure 8, confirming the behavior observed in Figure 7. In general, all metrics are improved by deconvolution methods compared to the TFM–except for amplitude estimation, because regularization introduces some bias in the estimated reflectivity. Deconv$_1$, however, performs quite poorly, since less than one half of the pairs of reflectors are resolved, with many positioning errors. Including the PSF variability strongly improve all criteria, which are still improved by accounting for the colored noise model. In particular, the resolving capability is 100%, with less positioning errors and better amplitude recovery than with Deconv$_4$. This method performs almost as well as the inversion on the FMC data–although it is much more efficient computationally, as will be shown in the next subsection.

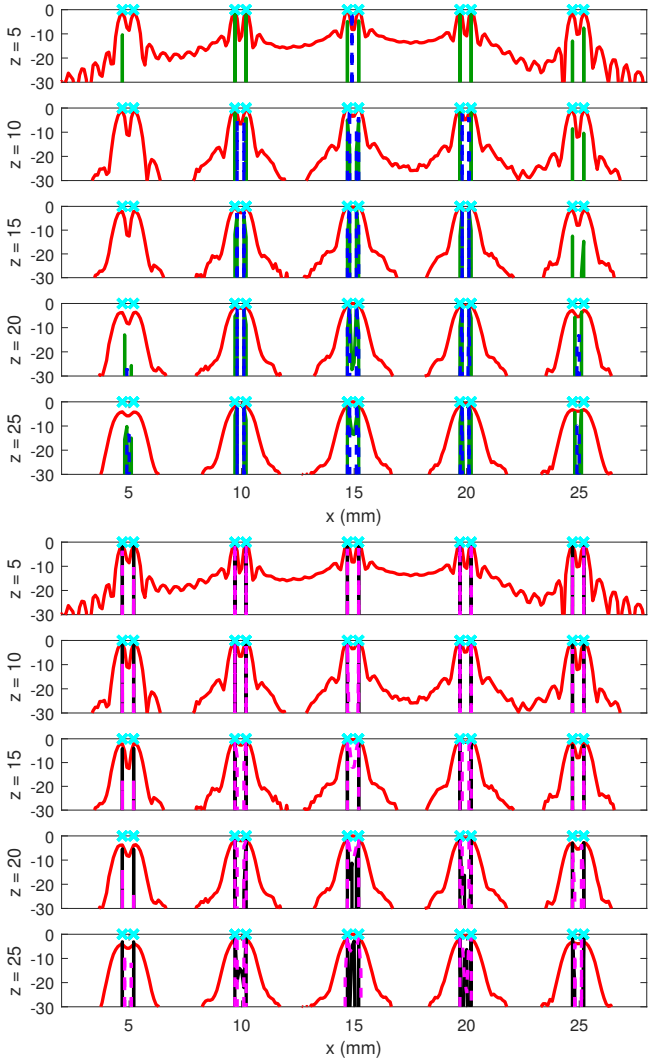

Fig. 7. Reconstruction results on synthetic data. Intensity lines (in dB) of reflectivity profiles at the depths of the five reflectors: TFM image (red line), Deconv$_1$ (blue stem), Deconv$_4$ (green stem), Deconv$_4^{\mathcal{W}}$ (magenta stem), and FMC inversion (black stem). The true locations are represented by the cyan crosses.

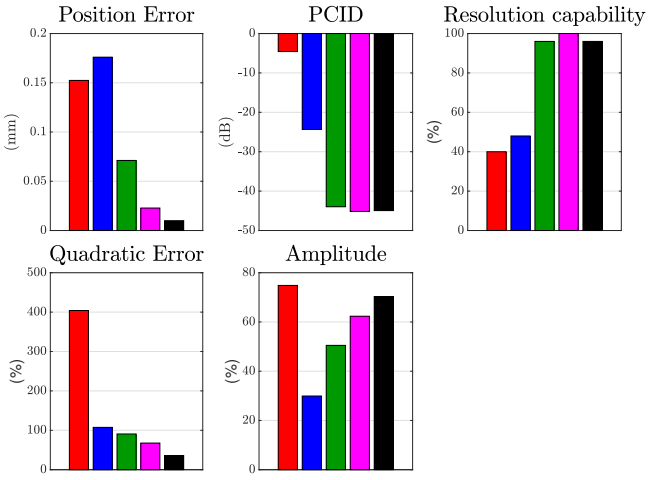

Fig. 8. Quantitative results with different metrics on synthetic data. TFM image (red), Deconv$_1$ (blue), Deconv$_4$ (green), Deconv$_4^{\mathcal{W}}$ (magenta), and FMC inversion (black).

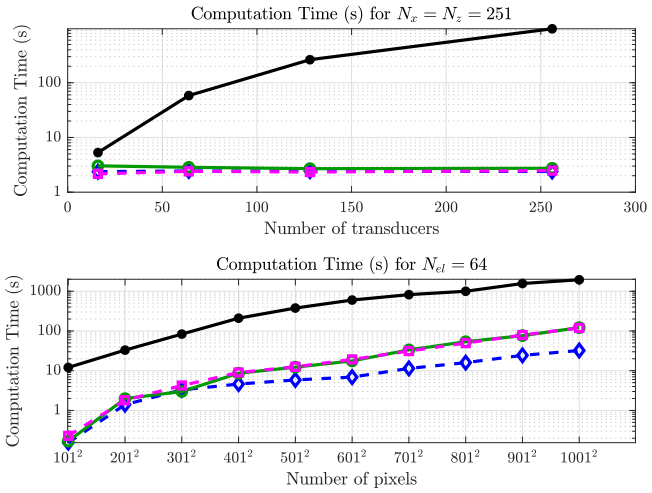

Fig. 9. Computation times for Deconv$_1$ (blue), Deconv$_4$ (green), Deconv$_4^{\mathcal{W}}$ (magenta), and FMC inversion (black). Top: as a function of the number of transducers, for a 251^2-pixel image. Bottom: as a function of the image size, with 64 transducers. Both ordinate axes are in logarithmic scale.

C. Computation times

Figure 9 shows the computation times for the different methods, as a function of the number of transducers and of the image size. Note that the TFM image, the reference PSFs, whitening filters and interpolating weights can be computed prior to optimization. Therefore, the corresponding computation time (typically a few seconds) is not considered here. All computation times have been evaluated on a laptop computer with 16.0 GB RAM, equipped with an Intel Core i7-7820 HK @ 2.90 GHz quad-core processor and a NVIDIA GeForce GTX 1080 graphics card.

As expected, the computational complexity of the different deconvolution methods does not depend on the number of transducers N_{el}, since all computations have been moved to the image space. This is obviously not the case for FMC inversion, where the data size is proportional to N_{el}^2. For a 251×251-pixel image, the computation time for Deconv$_4^{\mathcal{W}}$ is always about 2 seconds, while the time ratio between Deconv$_4^{\mathcal{W}}$ and FMC inversion varies from 3 (with 32 transducers) to 400 (with 256 transducers).

For all methods, the computation time increases similarly as a function of the image size. As expected, Deconv$_1$ is the fastest one. With 64 transducers, accounting for the PSF interpolation and the whitening procedure increases the computation time by a factor of 1.4 for the 101×101-pixel image (0.15 s vs. 0.23 s), and by a factor of 3.7 for the biggest, 1-million-pixel, one (32.2 s vs. 119.2 s). Finally, with 64 transducers, Deconv$_4^{\mathcal{W}}$ is approximately 30 times faster than FMC inversion, whatever the image size.

VII. Results with experimental data

The proposed method is now evaluated for the inspection of a stainless steel sample from Electric Power Research Institute (EPRI, Charlotte, North Carolina, USA). The experimental sample represented in Figure 10 is made of 304 stainless steel (sound speed $c = 5\,650$ m/s) and contains 41 close side-drilled holes (SDHs) with diameter 0.3 mm, approximately aligned around depth $z_{\text{SDH}} = 51.6$ mm. The center-to-center distance between SDHs regularly decreases from 2.55 mm (left) to 0.4 mm (right).

Fig. 10. Stainless steel block containing a set of 41 close aligned SDHs (⌀ 0.3 mm), with decreasing distance from left to right.

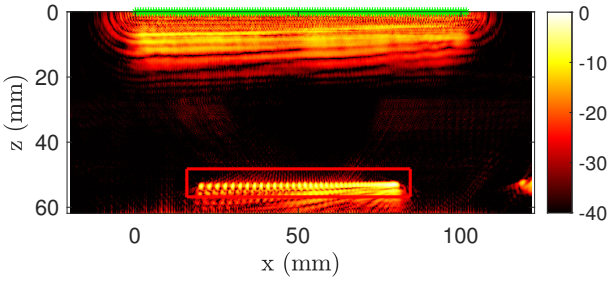

Fig. 11. TFM image reconstruction of the stainless steel block shown in Figure 10. Transducer locations are marked with green stars, and the reconstruction grid for inversion methods is framed in red.

FMC data have been acquired using the Pioneer platform from TPAC (West Chester, Ohio, USA). The probe is a 128-element probe designed by Imasonic (Voray-sur-l'Ognon, France), with central frequency equal to 3 MHz, and with an inter-element spacing equal to 0.8 mm. At this frequency, the wavelength is $\lambda = 1.88$ mm. The Rayleigh criterion, measuring the resolution limit of standard ultrasonic imaging methods [7], [16]–[18], is defined as: $\mathcal{R} := 0.61\lambda/\sin\theta$, with $\tan\theta = D/(2z_{\text{SDH}})$ and D the aperture of the probe. In this configuration setup, $\mathcal{R} = 1.64$ mm, which corresponds to the distance between the SDHs located at $x \approx 56$ mm. The TFM image of the full sample is shown in Figure 11, confirming this resolution limit.

Image reconstruction methods are applied on the area framed in red in Figure 11. The pixel size is 0.05×0.05 mm^2, so that the image dimension is $N_x \times N_z = 1373 \times 173$ pixels. The elementary waveform used in model (1) and in the generation of the reference PSFs is a Gaussian wavelet [32], whose parameters have been estimated by fitting the backwall echoes in the FMC data. It is represented in red on the A-scan signals in Figure 2. Due to the image geometry, we use three horizontally-aligned reference PSFs, that are shown in Figure 12 (a). Their size is $3\lambda \times 3\lambda$, which corresponds to 2D convolution kernels of 113×113 pixels.

The following methods are compared, whose names follow the denomination introduced in Section VI-A: TFM, Deconv$_1$, Deconv$_3$, and Deconv$_3^{\mathcal{W}}$. Their respective computation times are around 0.2, 9, 24 and 20 seconds. For all methods, the regularization parameters are set to $\mu_1 = 1.0\,\|\mathbf{H}^t \boldsymbol{o}_{\text{TFM}}\|_\infty$ and

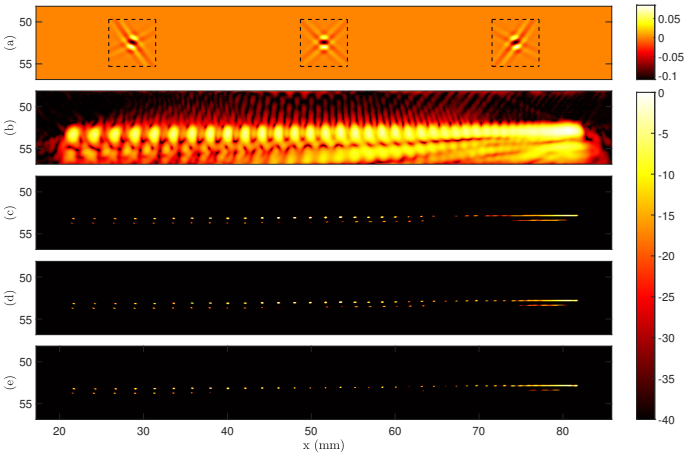

Fig. 12. Ultrasonic imaging of the stainless steel piece showed in Figure 10. (a): the three reference PSFs used in the interpolation method (the black frames show the considered spatial extension of the kernels). (b): TFM reconstruction. (c): reconstruction by Deconv_1. (d): reconstruction by Deconv_3. (e): reconstruction by $\text{Deconv}_3^{\mathcal{W}}$.

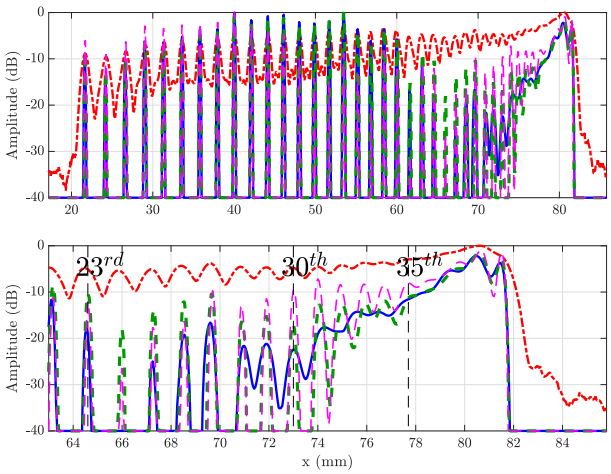

Fig. 13. Intensity lines (in dB) of the reconstructed reflectivity images in Figure 12, integrated in depth for $z = z_{\text{SDH}} \pm 0.6$ mm. TFM image (red, Deconv_1 (blue), Deconv_3 (green), and $\text{Deconv}_3^{\mathcal{W}}$ (magenta). Top: full x range. Bottom: zoom on the right side with the closest SDHs.

$\mu_2 = 10^{-4} \left\| \mathbf{H}^t \boldsymbol{o}_{\text{TFM}} \right\|_2$, with the forward model operator and the data adapted to the method (see the end of Section VI-A for more details).

The reconstructed images are displayed in Figure 12. For more precise analysis, intensity lines along the x direction are represented in Figure 13. For each x, the intensity is averaged over $z_{\text{SDH}} \pm 0.6$ mm. The TFM image shows many artifacts and, in particular, the right side of the image is hardly interpretable: the closest resolved SDHs (with PCID below -6 dB) are the 22^{nd} and 23^{rd} ones, located around $x \approx 65$ mm and distant from 1.4 mm. The image obtained by Deconv_1 achieves satisfactory detection and separation of the most distant SDHs, up to $x \approx 60$ mm. Then, some SDHs are missed. The last resolved SDH pair is located around $x \approx 73$ mm (29^{th} and 30^{th} ones, distant from 1.0 mm). Better separation is achieved by considering the shift-variant PSF interpolation model, in particular for $x \in [65, 80]$ mm. For Deconv_3, the last resolved SDHs pair is located around $x \approx 76$ mm (32^{nd} and 33^{rd}, distant from 0.7 mm). Both Deconv_1 and Deconv_3, however, show many artifacts below most flaws—see in particular for $x \leq 45$ mm and for $x \in [55, 65]$ mm in Figure 12. Considering both the PSF interpolation model and the whitening procedure, $\text{Deconv}_3^{\mathcal{W}}$ strongly reduces these artifacts, which are only visible at the two extremities of the reconstructed image, and still improves the resolution. The last resolved SDH with PCID below -6 dB is also the 33^{rd} one, but the PCID is around -5.5 dB between the 33^{rd} and 34^{th} SDHs, and between the 34^{rd} and 35^{th} ones. The closest resolved flaws with the proposed method are separated by 0.7 mm center to center (and by 0.4 mm edge to edge), which is more than four times smaller than the Rayleigh criterion.

VIII. Conclusion

Our contribution interprets the TFM image as a linear projection of the FMC data in the space domain. More precisely, it relies on a slowly varying, non-stationary blur model to mathematically describe the relation between the reflectivity map of the media and the TFM image. The spatially varying point spread function depends on both the geometrical and the acoustical configurations of the setup. We proposed a computationally efficient interpolation method to account for these spatial variations. We also proposed a whitening scheme to account for the fact that the TFM image contains spatially correlated, non-stationary noise. The latter is also based on an interpolation model, and its overhead computing cost is negligible.

The resulting non-stationary deconvolution method also relies on a sparsity assumption on the reflectivity map. In the synthetic data case, it produced results of similar quality as the reference inversion of FMC data. In the experimental data case, the method was able to separate close SDHs with a diameter six times smaller than the wavelength and distant from a quarter of the Rayleigh criterion.

In our interpolation model, offline computations (which are necessary to determine the reference PSFs, the whitening filters and the associated weights, for instance) can be performed in advance as far as the geometrical and acoustical configuration is known, which is often the case in industrial contexts. Under our current implementation, the proposed method cannot perform real time reconstructions. However, for a standard configuration of 64 transducers and 251×251 pixels, the online computation time is around one second using a rather standard laptop computer, which is still reasonable in some practical applications.

In practice, for more computational efficiency, we could imagine the following inspection strategy: first, the TFM image is computed. Second, if something suspicious is detected on the TFM image, the proposed method is applied to increase the quality of the reconstructed image. Similarly to what was performed in the experimental section of the paper, the reconstruction procedure could then be run only on parts of the inspected piece where high-resolution imaging is required.

Finally, let us mention that the current model assumes the shape invariance of the ultrasonic pulse during the propagation.

Significant distortions could occur in attenuative and dispersive materials [36]–[38]. Our ongoing research consists in incorporating such distortions in our spatially-varying PSF model, in order to adapt our non-stationary deconvolution method to such complex materials.

ACKNOWLEDGMENT

We would like to thank George D. Connolly from Electric Power Research Institute (EPRI, Charlotte, USA) who kindly lent us the experimental specimen.

This work was partially funded by the French ANRT (Association Nationale Recherche Technologie), project 2017/1083.

REFERENCES

[1] B. Drinkwater and P. Wilcox, "Ultrasonic arrays for non-destructive evaluation: A review," *NDT&E INT*, vol. 39, no. 7, pp. 525–541, Oct. 2006.

[2] M. Sutcliffe, M. Weston, B. Dutton, P. Charlton, and K. Donne, "Real-time full matrix capture for ultrasonic non-destructive testing with acceleration of post-processing through graphic hardware," *NDT&E INT*, vol. 51, pp. 16 – 23, 2012.

[3] M. Karaman, P.-C. Li, and M. O. Donnell, "Synthetic aperture imaging for small scale systems," *IEEE Transactions on Ultrasonics, Ferroelectrics, and Frequency Control*, vol. 42, no. 3, pp. 429–442, May 1995.

[4] G. Montaldo, M. Tanter, J. Bercoff, N. Benech, and M. Fink, "Coherent plane-wave compounding for very high frame rate ultrasonography and transient elastography," *IEEE Transactions on Ultrasonics, Ferroelectrics, and Frequency Control*, vol. 56, no. 3, pp. 489–506, Mar. 2009.

[5] M. Tanter and M. Fink, "Ultrafast imaging in biomedical ultrasound," *IEEE Transactions on Ultrasonics, Ferroelectrics, and Frequency Control*, vol. 61, no. 1, pp. 102–119, Jan. 2014.

[6] P. Wilcox, C. Holmes, and B. Drinkwater, "Advanced Reflector Characterization with Ultrasonic Phased Arrays in NDE Applications," *IEEE Transactions on Ultrasonics, Ferroelectrics, and Frequency Control*, vol. 54, no. 8, pp. 1541–1550, Aug. 2007.

[7] M. V. Felice and Z. Fan, "Sizing of flaws using ultrasonic bulk wave testing: A review," *Ultrasonics*, vol. 88, pp. 26–42, Aug. 2018.

[8] A. Chabot, N. Laroche, E. Carcreff, M. Rauch, and J.-Y. Hascoët, "Towards defect monitoring for metallic additive manufacturing components using phased array ultrasonic testing," *Journal of Intelligent Manufacturing*, vol. 31, no. 5, pp. 1191–1201, 2020.

[9] A.-F. Obaton, B. Butsch, E. Carcreff, N. Laroche, J. Tarr, and A. Donmez, "Efficient volumetric non-destructive testing methods for additively manufactured parts," *Welding in the World*, vol. 64, no. 8, pp. 1417–1425, 2020.

[10] J. Zhang, B. W. Drinkwater, P. D. Wilcox, and A. J. Hunter, "Defect detection using ultrasonic arrays: The multi-mode total focusing method," *NDT&E INT*, vol. 43, no. 2, pp. 123–133, Mar. 2010.

[11] L. J. Busse, H. D. Collins, and S. R. Doctor, "Review and discussion of the development of synthetic aperture focusing technique for ultrasonic testing (SAFT-UT)," Tech. Rep. NUREG/CR-3625, PNL-4957, 6977775, Mar. 1984.

[12] C. Holmes, B. Drinkwater, and P. Wilcox, "Post-processing of the full matrix of ultrasonic transmit-receive array data for non-destructive evaluation," *NDT&E INT*, vol. 38, no. 8, pp. 701–711, Dec. 2005.

[13] M. V. Felice, A. Velichko, and P. D. Wilcox, "Accurate depth measurement of small surface-breaking cracks using an ultrasonic array post-processing technique," *NDT&E INT*, vol. 68, pp. 105–112, Dec. 2014.

[14] K. Sy, P. Brédif, E. Iakovleva, O. Roy, and D. Lesselier, "Development of the specular echoes estimator to predict relevant modes for Total Focusing Method imaging," *NDT&E INT*, vol. 99, pp. 134–140, Oct. 2018.

[15] C. Peng, L. Bai, J. Zhang, and B. W. Drinkwater, "The sizing of small surface-breaking fatigue cracks using ultrasonic arrays," *NDT&E INT*, vol. 99, pp. 64–71, Oct. 2018.

[16] F. Simonetti, "Multiple scattering: The key to unravel the subwavelength world from the far-field pattern of a scattered wave," *Phys. Rev. E*, vol. 73, no. 3, Mar. 2006.

[17] ——, "Localization of pointlike scatterers in solids with subwavelength resolution," *Applied Physics Letters*, vol. 89, no. 9, pp. 094–105, Aug. 2006.

[18] C. Fan, M. Caleap, M. Pan, and B. W. Drinkwater, "A comparison between ultrasonic array beamforming and super resolution imaging algorithms for non-destructive evaluation," *Ultrasonics*, vol. 54, no. 7, pp. 1842–1850, Sep. 2014.

[19] N. Laroche, S. Bourguignon, E. Carcreff, J. Idier, and A. Duclos, "An inverse approach for ultrasonic imaging from full matrix capture data. application to resolution enhancement in NDT," *IEEE Transactions on Ultrasonics, Ferroelectrics, and Frequency Control*, vol. 67, no. 9, pp. 1877–1887, 2020.

[20] J. Jensen, S. Nikolov, K. Gammelmark, and M. Pedersen, "Synthetic aperture ultrasound imaging," *Ultrasonics*, vol. 44, pp. e5–e15, Dec. 2006.

[21] A. Tuysuzoglu, J. M. Kracht, R. Cleveland, M. Çetin, and W. Karl, "Sparsity driven ultrasound imaging," *The Journal of the Acoustical Society of America*, vol. 131, no. 2, pp. 1271–1281, Feb. 2012.

[22] G. Guarneri, D. Pipa, F. Junior, L. de Arruda, and M. Zibetti, "A Sparse Reconstruction Algorithm for Ultrasonic Images in Nondestructive Testing," *Sensors*, vol. 15, no. 4, pp. 9324–9343, Apr. 2015.

[23] P. R. Bueno, M. V. W. Zibetti, and J. M. Maia, "Real-time ultrasound image reconstruction as an inverse problem on a GPU," *Journal of Real-Time Image Processing*, Jul. 2018.

[24] T. Szasz, A. Basarab, and D. Kouame, "Beamforming Through Regularized Inverse Problems in Ultrasound Medical Imaging," *IEEE Transactions on Ultrasonics, Ferroelectrics, and Frequency Control*, vol. 63, no. 12, pp. 2031–2044, Dec. 2016.

[25] E. Ozkan, V. Vishnevsky, and O. Goksel, "Inverse Problem of Ultrasound Beamforming With Sparsity Constraints and Regularization," *IEEE Transactions on Ultrasonics, Ferroelectrics, and Frequency Control*, vol. 65, no. 3, pp. 356–365, Mar. 2018.

[26] O. Michailovich, "A Novel Approach to the 2-D Blind Deconvolution Problem in Medical Ultrasound," *IEEE Transactions on Medical Imaging*, vol. 24, pp. 86–104, 2005.

[27] M. I. Florea, A. Basarab, D. Kouame, and S. A. Vorobyov, "An Axially Variant Kernel Imaging Model Applied to Ultrasound Image Reconstruction," *IEEE Signal Processing Letters*, vol. 25, no. 7, pp. 961–965, 2018.

[28] A. Besson, L. Roquette, D. Perdios, M. Simeoni, M. Arditi, P. Hurley, Y. Wiaux, and J.-P. Thiran, "A Physical Model of Non-stationary Blur in Ultrasound Imaging," *IEEE Transactions on Computational Imaging*, vol. 5, no. 3, pp. 381–394, 2019.

[29] M. Gentile, F. Courbin, and G. Meylan, "Interpolating point spread function anisotropy," *Astronomy & Astrophysics*, vol. 549, p. A1, Jan. 2013.

[30] L. Denis, E. Thiébaut, F. Soulez, J.-M. Becker, and R. Mourya, "Fast Approximations of Shift-Variant Blur," *International Journal of Computer Vision*, vol. 115, no. 3, pp. 253–278, Dec. 2015.

[31] P. R. Stepanishen, "Transient Radiation from Pistons in an Infinite Planar Baffle," *The Journal of the Acoustical Society of America*, vol. 49, no. 5B, pp. 1629–1638, May 1971.

[32] R. Demirli and J. Saniie, "Model-based estimation of ultrasonic echoes. Part I: Analysis and algorithms," *IEEE Transactions on Ultrasonics, Ferroelectrics, and Frequency Control*, vol. 48, no. 3, pp. 787–802, May 2001.

[33] B. Friedlander, "System identification techniques for adaptive signal processing," *Circuits, Systems, and Signal Processing*, vol. 1, no. 1, pp. 3–41, 1982.

[34] A. Kessy, A. Lewin, and K. Strimmer, "Optimal Whitening and Decorrelation," *The American Statistician*, vol. 72, no. 4, pp. 309–314, 2018.

[35] A. Beck and M. Teboulle, "A Fast Iterative Shrinkage-Thresholding Algorithm for Linear Inverse Problems," *SIAM Journal on Imaging Sciences*, vol. 2, no. 1, pp. 183–202, 2009.

[36] A. C. Kak and K. A. Dines, "Signal Processing of Broadband Pulsed Ultrasound: Measurement of Attenuation of Soft Biological Tissues," *IEEE Transactions on Biomedical Engineering*, vol. BME-25, no. 4, pp. 321–344, 1978.

[37] S. Flax, "Spectral characterization and attenuation measurements in ultrasound," *Ultrasonic Imaging*, vol. 5, no. 2, pp. 95–116, 1983.

[38] E. Carcreff, S. Bourguignon, J. Idier, and L. Simon, "A linear model approach for ultrasonic inverse problems with attenuation and dispersion," *IEEE Transactions on Ultrasonics, Ferroelectrics, and Frequency Control*, vol. 61, no. 7, pp. 1191–1203, Jul. 2014.